



Electron Mobility in $\text{-Al}_2\text{O}_3/\text{SrTiO}_3$

Christensen, Dennis Valbjørn; Frenkel, Y.; Schutz, P.; Trier, Felix; Wissberg, S.; Claessen, R.; Kalisky, B.; Smith, Anders; Chen, Yunzhong; Pryds, Nini

Published in:
Physical Review Applied

Link to article, DOI:
[10.1103/PhysRevApplied.9.054004](https://doi.org/10.1103/PhysRevApplied.9.054004)

Publication date:
2018

Document Version
Peer reviewed version

[Link back to DTU Orbit](#)

Citation (APA):
Christensen, D. V., Frenkel, Y., Schutz, P., Trier, F., Wissberg, S., Claessen, R., ... Pryds, N. (2018). Electron Mobility in $\text{-Al}_2\text{O}_3/\text{SrTiO}_3$. *Physical Review Applied*, 9(5), [054004]. DOI: 10.1103/PhysRevApplied.9.054004

General rights

Copyright and moral rights for the publications made accessible in the public portal are retained by the authors and/or other copyright owners and it is a condition of accessing publications that users recognise and abide by the legal requirements associated with these rights.

- Users may download and print one copy of any publication from the public portal for the purpose of private study or research.
- You may not further distribute the material or use it for any profit-making activity or commercial gain
- You may freely distribute the URL identifying the publication in the public portal

If you believe that this document breaches copyright please contact us providing details, and we will remove access to the work immediately and investigate your claim.

Electron mobility in $\gamma\text{-Al}_2\text{O}_3/\text{SrTiO}_3$

D. V. Christensen^{1,a)}, Y. Frenkel², P. Schütz³, F. Trier¹, S. Wissberg², R. Claessen³, B. Kalisky², A. Smith¹, Y. Z. Chen¹, and N. Pryds¹

¹*Department of Energy Conversion and Storage, Technical University of Denmark, Risø Campus, DK-4000 Roskilde, Denmark*

²*Department of Physics and Institute of Nanotechnology and Advanced Materials, Bar-Ilan University, 5290002 Ramat-Gan, Israel*

³*Physikalisches Institut and Röntgen Center for Complex Material Systems (RCCM), Universität Würzburg, Am Hubland, 97074 Würzburg, Germany*

a) Corresponding author – dechr@dtu.dk

Abstract:

One of the key issues in engineering oxide interfaces for electronic devices is achieving high electron mobility. SrTiO_3 -based interfaces with high electron mobility have attracted a lot of interest due to the possibility of combining quantum phenomena with the many functionalities exhibited by SrTiO_3 . To date, the highest electron mobility ($140,000 \text{ cm}^2/\text{Vs}$ at 2 K) is obtained by interfacing perovskite SrTiO_3 with spinel $\gamma\text{-Al}_2\text{O}_3$. The origin of the high mobility, however, remains poorly understood. Here, we investigate the scattering mechanisms limiting the mobility in $\gamma\text{-Al}_2\text{O}_3/\text{SrTiO}_3$ at temperatures between 2 and 300 K and over a wide range of sheet carrier densities. For $T > 150 \text{ K}$, we find that the mobility is limited by longitudinal optical phonon scattering. For large sheet carrier densities ($> 8 \cdot 10^{13} \text{ cm}^{-2}$) the screened electron-phonon coupling leads to room temperature mobilities up to $\mu \sim 12 \text{ cm}^2/\text{Vs}$. For $5 \text{ K} < T < 150 \text{ K}$, the mobility scales as $\sim T^{-2}$ consistent with electron-electron scattering limiting the electron mobility. For $T < 5 \text{ K}$ and at an optimal sheet carrier density of $\sim 4 \cdot 10^{14} \text{ cm}^{-2}$, the electron mobility is found to exceed $100,000 \text{ cm}^2/\text{Vs}$. At sheet carrier densities less than the optimum, the electron mobility decreases rapidly and the current flow becomes highly influenced by domain walls and defects in the near-interface region of SrTiO_3 . At carrier densities higher than the optimum, the SrTiO_3 heterostructure gradually becomes bulk conducting and the electron mobility decreases to $\sim 20,000 \text{ cm}^2/\text{Vs}$. We argue that the high electron mobility observed arises from a spatial separation of donors and electrons with oxygen vacancy donors preferentially forming at the interface whereas the itinerant electrons extend deeper into SrTiO_3 . Understanding the scattering mechanism in $\gamma\text{-Al}_2\text{O}_3/\text{SrTiO}_3$ paves the way for creation of high-mobility nanoscale electronic devices.

Keywords: $\gamma\text{-Al}_2\text{O}_3/\text{SrTiO}_3$; Electron Mobility, Two-dimensional electron gas, Oxide Electronics; Polarons

Introduction:

Achieving high electron mobility is a pivot of material research. In particular, it is paramount for application in efficient electronic components and studying quantum phenomena. A large Hall mobility, $\mu = e\tau/m^*$, is realized by either a low effective mass (m^*) or a long momentum relaxation time (τ). For instance, the pioneering work on $\text{Al}_x\text{Ga}_{1-x}\text{As}/\text{GaAs}$ heterostructures led to a record-high electron mobility of $\mu \sim 3.6 \cdot 10^7 \text{ cm}^2/\text{Vs}$ at 0.36 K through combination of a low effective mass of $m_{\text{GaAs}}^* \sim 0.06m_e$ and improvements in τ [1]. In contrast, $\text{Mg}_x\text{Zn}_{1-x}\text{O}/\text{ZnO}$ with $\mu \sim 1.3 \cdot 10^6 \text{ cm}^2/\text{Vs}$ at 0.1 K [2] and SrTiO_3 -based heterostructures with $\mu \sim 1.4 \cdot 10^5 \text{ cm}^2/\text{Vs}$ at 2 K [3] both exhibit high mobilities at low temperatures despite being characterized by large effective masses of $m_{\text{ZnO}}^* \sim 0.3m_e$ and $m_{\text{STO}}^* \sim 1m_e$. The high electron mobility in $\text{Mg}_x\text{Zn}_{1-x}\text{O}/\text{ZnO}$ is achieved by reducing the defect scattering. This is accomplished using molecular beam epitaxy (MBE) leading to a crystal quality close to that of traditional semiconductors. SrTiO_3 (STO), however, typically contains a large amount of impurities [4], but the large dielectric constant at low temperatures [5, 6] counteracts the interaction between electrons and ionized scattering sites. The forgiving nature of the STO crystal together with the manifold of physical phenomena observed in STO and STO-based heterostructures have fueled the recent interest in achieving high mobility.

At room temperature the electron mobility in doped STO is typically $1\text{-}12 \text{ cm}^2/\text{Vs}$ and generally believed to be limited by electron-electron interactions or longitudinal optical phonon scattering [7–9]. At temperatures below 5 K, the mobility in bulk, doped STO substrates reaches a value of $\sim 22,000 \text{ cm}^2/\text{Vs}$ with static, ionized scattering sites being the limiting factor [9]. Various strategies have been utilized in the search for high mobility in STO and STO-based heterostructures, including MBE thin film growth [10], strain [11], delta doping [12, 13], modulation doping [14], surface passivation [15] and defect engineering [14, 16]. To date, the largest mobility of $140,000 \text{ cm}^2/\text{Vs}$ has been observed when STO is interfaced with $\gamma\text{-Al}_2\text{O}_3$ (GAO) [3], where oxygen vacancies account for the formation of the interface conductivity [3, 17, 18]. Contrary to the majority of other STO-based heterostructures [19, 20], the highest mobilities in GAO/STO surprisingly occur at a high sheet carrier density exceeding 10^{14} cm^{-2} , despite the abundance of oxygen vacancy donors in STO, which act as scattering sites [3, 18, 21]. A spatial separation of the electrons and donors within STO was recently proposed to be the origin of the high mobility in GAO/STO at low temperatures [21], but it remains to be settled unambiguously. In addition, the dominant scattering mechanisms in GAO/STO at intermediate and high temperatures have yet to be identified.

Here, we investigate the electron mobilities of GAO/STO heterostructures over a wide range of carrier densities, which were obtained by controlling the density of oxygen vacancies via a variation of growth parameters or post-growth annealing in oxygen at elevated temperatures ($\sim 200 \text{ }^\circ\text{C}$). We show that the carrier density can be used as a handle to tune the mobility, electron-phonon coupling and effective mass at room temperature. In addition, we use transport and scanning superconducting quantum interference device (SQUID) measurements to probe the relationship between the mobility, carrier density, current flow and scattering at low temperature. The study opens a path towards designing all-oxide quantum devices and extraordinary magnetoresistive devices.

Methods:

The transport data of the GAO/STO samples presented here is a compilation of three sets of measurements: The transport data from the first set was taken from Ref. [3], where the GAO/STO samples were produced using pulsed laser deposition (PLD) at a temperature of 600 °C, a laser fluence of 1.5 J/cm² and an oxygen partial pressure of 10⁻⁴ mbar. The changes in the carrier densities and mobilities occurred due to a variation of the GAO film thickness between 2 and 4 unit cells, with the largest mobility occurring at 2.5 unit cell. In the second set of samples, we grew more than 40 GAO/STO heterostructures using PLD, but in another growth chamber. Here, high mobility was obtained by growing approximately 3.5 unit cells of GAO at 650 °C with a fluence of 3.8 J/cm² in a growth pressure of 10⁻⁵ mbar. Changes in the carrier density and mobility were primarily obtained by varying the growth pressure from 10⁻⁴ mbar to 10⁻⁶ mbar with a lowering of the pressures causing a higher carrier density. In the third set of measurements, a GAO/STO sample was produced with the same deposition conditions as the second set with a pressure of 2·10⁻⁵ mbar. Several sequential post-deposition annealing steps were then used to change the carrier density and mobility by annihilation of the oxygen vacancy donors. Here, the transport properties were measured after annealing the sample in ~200 °C in 1 bar oxygen for 2-8 hours at each step. The sheet resistance was measured during the annealing process, as this allowed us to estimate the change in the carrier density. The duration of the annealing was between 2 and 8 hours (typically 6 hours) according to when a desired change in the carrier density had occurred. More details on changing the carrier density systematically using post-deposition annealing of GAO/STO with *in-situ* transport measurements can be found in Ref. [18]. In all cases, GAO was deposited on STO with a TiO₂-termination obtained using the same protocol described elsewhere [22]. The carrier density and mobility were determined from the slope of the Hall coefficients at low magnetic fields in the van der Pauw geometry. We note that for the high carrier density samples, the Hall coefficient was non-linear as a function of the magnetic field for $T < 40$ K with the steepest slope occurring at high magnetic fields. This behavior is in contrast to LAO/STO at carrier densities above the Lifshitz carrier density ($n_s \sim 1.7 \cdot 10^{13}$ cm⁻²), where the Hall coefficient has the steepest slope at low fields due to transport occurring in two *n*-type bands [23]. As it will be discussed elsewhere, we attribute the non-linear Hall coefficient observed for GAO/STO at high carrier densities to a non-saturating anomalous Hall coefficient, which scales linearly with the magnetoresistance (MR). In this case, the carrier density is most accurately determined from the Hall coefficient at low magnetic fields where the magnetoresistance varies slowly as B^2 . The use of the low-field Hall coefficient to extract the carrier density is consistent with previous reports on GAO/STO [3]. As shown in Figure 1 and Figure 2 this led to (i) a temperature independent carrier density and (ii) $\mu \propto T^{-2}$ for 5 K < T < 150 K, which is consistent with that observed in other bulk STO and STO-based heterostructures. Note that if one used the high-field Hall coefficient to extract the carrier density (as appropriate if the anomalous Hall coefficient is saturating or within the 2-band model to deduce the total carrier density), it would lead to (i) a decrease of the total itinerant carrier density below 40 K, (ii) an effective mobility exceeding 300,000 cm²/Vs and (iii) large deviations of the T^{-2} behavior.

The current density was imaged using a scanning SQUID. An alternating current was driven through the sample, which produces a magnetic flux picked up by a pickup loop of diameter 1.8 μm. The pickup loop was connected to a SQUID, which measured the magnetic flux with lock-in detection. By scanning the pickup-loop along the sample surface, a two-dimensional map of the magnetic flux could be measured. The measured flux is given by $\phi_s = \int g(x, y) \vec{B} \cdot d\vec{a}$ where the integral is taken over the plane of the pickup loop, $g(x, y)$ is the point spread function of the pickup loop, \vec{B} is the magnetic field produced by

the current in the sample and $d\vec{a}$ is the infinitesimal area vector element pointing normal to the plane of the pickup loop (i.e. along z). Each flux image is a convolution of the z -component of the magnetic field and the SQUID point spread function. A current carrying wire produces circulating magnetic field around it therefore will appear in our images as a black stripe next to a white stripe.

Temperature dependence of the mobility:

Figure 1 shows the sheet resistance, carrier density and mobility in a GAO/STO heterostructure after six annealing steps, each comprising storage in 1 bar oxygen at ~ 200 °C for 2-8 hours. Changes in the transport properties were probed *in situ* by measuring the sheet resistance during the annealing process (see Methods and Ref. [18] for more details). The annealing lowers the carrier density monotonically and drives the sample from a metallic to an insulating state. The mobility decreases systematically over the whole temperature range from 2 K to 300 K with the most prominent change below 30 K and less pronounced changes near room temperature. In the following, we first identify the contributions to the mobility in order to fit its temperature dependence, and then discuss the corresponding scattering mechanisms at the various temperatures in detail.

The temperature dependence of the mobility (μ) in STO and STO-based heterostructures is assumed to be described by the Matthiessen rule [24],

$$\mu^{-1} = \sum_i \mu_i^{-1} \quad (1)$$

where each scattering mechanism has an associated temperature-dependent mobility contribution $\mu_i(T)$.

In the low-temperature regime ($T < 5$ K), the dominant scattering of electrons in STO and STO-based heterostructures is attributed to ionized impurities in STO [9], ionized donors [25] or surface roughness scattering [26]. The mobility contribution in this temperature regime, $\mu_{\text{low } T}$, is often taken to be temperature independent [7, 25], and for simplicity we will do the same here, $\mu_{\text{low } T} = \mu_{T \rightarrow 0 \text{ K}}$, and discuss the scattering mechanism later.

For $5 \text{ K} < T < 150 \text{ K}$, the dominant scattering mechanism remains unsettled even for bulk STO despite of intensive research. The change in mobility has been explained by the low-temperature scattering mechanism with a temperature dependent dielectric constant [26], acoustic phonon scattering [25], transverse optical phonon scattering [25], longitudinal optical (LO) phonon scattering [26], temperature dependent polaron properties [27] or electron-electron scattering [7]. Consistent with previous studies on STO and other STO-based heterostructures, we achieve a good agreement if we describe the mobility contribution with $\frac{1}{AT^m}$ in the intermediate temperature regime with A being a temperature-independent coefficient and $m \sim 2$. As discussed later, this is suggestive of electron-electron scattering being dominant in this temperature interval.

For $150 \text{ K} < T < 300 \text{ K}$, the limiting factor for the mobility has been attributed to electron-electron interactions [7], temperature-dependent transmission coefficients in Landauer channels connecting dopants [28] or LO phonon scattering [7–9]. The temperature dependence of the electron-electron contribution follows a $\sim T^{-2}$ behavior [7], whereas the scattering from a LO phonon with frequency ω_{LO}

is $\mu_{LO} \propto \exp\left(\frac{\hbar\omega_{LO}}{k_B T}\right)$. Hence, a hallmark to discriminate between the two contributions is the presence of a non-linearity when $\log(\mu)$ is plotted as a function of $\log(T)$. Such a non-linearity can be seen for $T > 150$ K as a deviation from the $\sim T^2$ behavior of the sheet resistance (Figure 1) and the $\sim T^{-2}$ behavior of the mobility (Figure 1 and Figure 2), respectively. We therefore use an expression for the longitudinal optical phonon scattering in the weak/intermediate coupling regime where the electron phonon coupling constant α is less than 6 [29]:

$$\mu_{LO} = \frac{\hbar}{2\alpha\hbar\omega_{LO}} \frac{e}{m_b} \left(\frac{m_b}{m_p}\right)^3 f(\alpha) \exp\left(\frac{\hbar\omega_{LO}}{k_B T}\right) \quad (2)$$

Here, $f(\alpha)$ is a monotonic function of α that varies slowly from 1 to 1.35 as α increases from 0 to 6 [29]. The bare effective mass is taken to be $m_b \sim 0.6m_e$ with m_e being the free electron mass [30]. As the electron moves through the lattice, it attracts positive ions leading to an enhanced effective mass described by the polaron effective mass m_p . For three-dimensional Fröhlich polaron [29], $m_p = m_b(1 + \alpha/6)$, whereas a two-dimensional electron gas with Fröhlich interactions to a three-dimensional lattice [31] leads to $m_p = m_b(1 + (\pi/8)\alpha + 0.1272\alpha^2)$. The dimensionality of the electron gas in STO-based heterostructures is dependent on the carrier density and growth conditions [32], but we here assume two-dimensional polarons consistent with a mobility study in LAO/STO [26]. We note that in 1953 Low and Pines published a similar expression [33] with $\mu_{LO} \propto (m_b/m_p)^2$, which is often used to describe the mobility in STO, but in 1955 the same authors published the above expression with $\mu_{LO} \propto (m_b/m_p)^3$ along with a short discussion on the discrepancy (see footnote 8 in Ref. [29]).

Cubic STO contains three LO phonons modes with energies $\hbar\omega_{LO1} = 21.4$ meV, $\hbar\omega_{LO2} = 58.6$ meV and $\hbar\omega_{LO3} = 100.1$ meV and corresponding coupling constants $\alpha_{LO1} = 0.009$, $\alpha_{LO2} = 0.47$ and $\alpha_{LO3} = 1.83$ reported by Barker [34]. We add the contribution from the three phonon modes according to Matthiessen's rule to obtain the total contribution of the longitudinal optical phonons, $\mu_{LO \text{ total}}$.

To conclude, we can express the total electron mobility as

$$\frac{1}{\mu(T)} = \frac{1}{\mu_{T \rightarrow 0}} + \frac{1}{AT^{-2}} + \frac{1}{\mu_{LO \text{ total}}(T)} \quad (3)$$

Using the two free parameters $\mu_{T \rightarrow 0 \text{ K}}$ and A , we find a good agreement with the experimental mobility in GAO/STO as observed in Figure 2. With a slight adjustment of α_{LO3} as described below, a similar agreement is found for all tested GAO/STO mobilities, including those in Figure 1, with low temperature mobilities ranging from 1000 to 100,000 cm^2/Vs and Hall sheet carrier densities between 10^{13} and 10^{15} cm^{-2} . In the following, we discuss the individual temperature regimes in detail.

Mobility at room temperature:

The electron mobility at room temperature is important for device application. From Figure 2 we deduce that the room temperature electron mobility is primarily limited by scattering from LO3 phonons. This is in contrast to Ref. [7] where electron-electron scattering is found to be dominating in GdTiO₃/STO heterostructures and heavily doped STO, but consistent with a number of other studies on bulk STO and STO-based heterostructures [7–9]. We have obtained the room temperature mobility for a number of

samples with varying carrier density achieved through either annealing or variation of deposition parameters (see Figure 3). The latter parameter variation encompasses samples from this study as well as from a previous study done by Chen et al [3]. All three sample series give consistent results. The lowest measured electron mobility ($\sim 2 \text{ cm}^2/\text{Vs}$) occurs at low carrier densities ($n_s \sim 4 \cdot 10^{12} \text{ cm}^{-2}$) after annealing and is consistent with the low electron mobilities of slightly reduced bulk STO [35, 36]. The highest electron mobilities ($\sim 12 \text{ cm}^2/\text{Vs}$) are obtained for high sheet carrier densities ($n_s > 8 \cdot 10^{13} \text{ cm}^{-2}$). The positive correlation between the room temperature mobility and the carrier density may be understood by investigating the carrier density dependence of Eq. (2). From angle resolved photoemission spectroscopy (ARPES) studies [27, 30] of the polaronic satellite feature, ω_{LO3} was found to be negligibly dependent on the carrier density. As the bare band effective mass is not expected to vary significantly with the carrier density, the only strong carrier density dependence therefore enters the expression for μ_{LO} (Eq. (2)) through the electron-phonon coupling constant $\alpha(n_s)$. Note that $m_p(\alpha(n_s))$ and $f(\alpha(n_s))$ inherits this density dependence. We can write out the dependence on α in Eq. (2) explicitly:

$$\mu_{LO}(\alpha) = \frac{\hbar}{2\alpha\hbar\omega_{LO}} \frac{e}{m_b} \left(1 + \left(\frac{\pi}{8}\right)\alpha + 0.1272\alpha^2 \right)^{-3} f(\alpha) \exp\left(\frac{\hbar\omega_{LO}}{k_B T}\right) \quad (4)$$

where $\mu_{LO}(\alpha)$ is plotted in the inset of Figure 3 using $m_b = 0.6m_e$. Inverting this function numerically to obtain $\alpha(\mu_{LO})$ allows one to deduce the electron-phonon coupling constant and corresponding polaron effective mass from the measured mobility as presented in the bottom panel of Figure 3. The electron-phonon coupling ranges from 2.8 at low carrier densities to 2 at high carrier densities and are similar to literature values of 2.6 [8] and 1.83 [34] and ARPES results [30] at 20 K where the coupling ranges from 2.8 to 1.3 upon increasing the carrier density from $4 \cdot 10^{13}$ to $9 \cdot 10^{13} \text{ cm}^{-2}$. Our deduced effective polaron mass changes from $1.8m_e = 3m_b$ to $1.4m_e = 2.3m_b$ upon increasing the carrier density, in good agreement with Nb-doped STO having an effective mass of $\sim 3m_b$ for 0.1% Nb-doping and a saturation at $\sim 2m_b$ above 1% Nb-doping [37].

Based on this analysis, we conclude that the high mobility at room temperature occurs at high carrier densities where the electron-phonon coupling is weak due to screening from electrons [30]. The reduced coupling results in less scattering and a lower effective mass.

Mobility at intermediate temperatures:

At intermediate temperatures, $T_{low} < T < 150 \text{ K}$, the mobility varies as $\sim T^{-2}$ independent of the carrier density with $T_{low} \sim 5 \text{ K}$ for high-mobility samples and $T_{low} \sim 30 \text{ K}$ for low-mobility samples. The mobility in this temperature range cannot be explained satisfactorily by scattering from a single branch of acoustic phonons, $\mu \sim T^{-1}$, or non-polar optical phonons with frequency ω_{TO} , $\mu \sim e^{\hbar\omega_{TO}/k_B T}$, using the expressions from Ref. [24]. The scattering could, in principle, be caused by a combination of several different scattering mechanisms, but this seems unlikely since the mobility scales with the carrier density in the same way ($\mu \propto n_s^{0.28 \pm 0.04}$) in the entire temperature interval $30 \text{ K} < T < 150 \text{ K}$. As the scaling is significantly different from that at low temperatures (see the following section), the changes in the mobility at intermediate temperatures appears not to be governed by the temperature-dependent dielectric constant either. In contrast, the T^{-2} -dependence in STO-based systems has been explained by electron-electron scattering [7, 37–39]. In the classical picture, the Hall electron mobility is unaffected

by collisions between two electrons if the velocity (and hence the total charge current) is preserved. Momentum can, however, be transferred to the lattice during an electron-electron scattering event for instance if the scattering process involves phonons. The microscopic mechanism and characteristics of the electron-electron scattering process has been a subject of several studies [37–41], but a unifying picture remains elusive for STO. In particular, deviations from Fermi-liquid behavior has been shown to occur [38], and another study advice against readily using the $\mu \propto T^{-2}$ scaling as evidence for electron-electron scattering [41].

Mobility at low temperatures:

At low temperatures, a high mobility of up to 22,000 cm²/Vs can be obtained in bulk conducting STO owing to the large dielectric constant [9]. Given optimized growth parameters (which may differ from one chamber to another), the electron mobility at the GAO/STO heterointerface may significantly exceed this value. In our previous results, Chen et al. reported the highest electron mobility when 2.5 unit cells GAO was deposited at 600 °C using pulsed laser deposition with a high laser fluence of 1.5 J/cm² in an oxygen pressure of 10⁻⁴ mbar [3]. In this study, high electron mobility was instead found when depositing ~3.5 unit cells GAO at 650 °C with a fluence of 3.8 J/cm² and a pressure of 10⁻⁵ mbar. The α -Al₂O₃ single crystalline target, substrate supplier and TiO₂-termination process were identical to that of used by Chen et al [3]. Using a fixed GAO thickness (2.5 u.c. or 3.5 u.c.) and a high laser fluence, the high carrier density and mobility are primarily obtained by optimizing the oxygen partial pressure. At low carrier densities ($\sim 10^{13}$ cm⁻²), the mobility at 2 K is of the order of 1000 cm²/Vs (see Figure 4) and similar to typical mobilities in LAO/STO [20]. At even lower densities, the interface undergoes a metal-to-insulator transition, which impedes the reliable determination of the low temperature electron mobility. Increasing the carrier density results in a pronounced increase in the mobility roughly described by $\mu \sim n_s^{1.5}$ until the mobility peaks at more than 100,000 cm²/Vs when the carrier density reaches $n_s(\mu_{max}) \sim 4 \cdot 10^{14}$ cm⁻². The positive correlation between the mobility and carrier density in GAO/STO is radically different from LAO/STO where the exponent is negative [19, 20]. Interestingly, a positive exponent of ~ 1.5 is also observed in modulation doped electronic systems where the donors and electrons are spatially separated [42, 43]. Heterostructures fabricated close to this mobility peak typically have a room temperature sheet resistance of ~ 1 k Ω and a large residual resistance ratio of $R_s(300\text{ K})/R_s(2\text{ K}) \sim 10,000$, consistent with the four orders of magnitude mobility enhancement upon cooling from $T = 300$ K or $T = 2$ K. The room temperature sheet resistance or the residual resistance ratio can often be used as a tool for fast screening of high-mobility samples during growth optimization.

Increasing the carrier density beyond $\sim 4 \cdot 10^{14}$ cm⁻² results in a gradual conversion into bulk three-dimensional conductivity of the STO substrate. Here, samples with $n_s > 3 \cdot 10^{15}$ cm⁻² represent the extreme case where the conductivity measured on the backside of the 0.5 mm thick STO substrate does not differ from that measured at the interface. In this case, the samples can be viewed as a homogeneously conducting 0.5 mm thick sheet with a 3D carrier density of $n_s/0.05\text{ cm} = 6 \cdot 10^{16}$ cm⁻³. The mobility decreases to $\sim 20,000$ cm²/Vs, which is consistent with bulk conducting STO with a similar three-dimensional carrier density formed by introducing donors throughout STO [32].

To investigate whether low- and high-mobility in GAO/STO heterostructures have distinct signatures in the spatial distribution of the current flow on the microscale, we investigated GAO/STO with varying

carrier densities and mobilities using a scanning superconducting quantum interference device (SQUID). Here, an alternating current in the sample creates a magnetic field, which is detected by the SQUID through a pick-up loop with a diameter of 1.8 μm . Our SQUID images (see Figure 4) show a qualitative difference in the spatial distribution of current flow between samples with low and high carrier density with a threshold of $\sim 3 \cdot 10^{14} \text{ cm}^{-2}$. At low electron densities ($\leq 1 \cdot 10^{14} \text{ cm}^{-2}$), we see striped modulations of the current flow, similar to previous reports in LAO/STO [44, 45]. The orientations of the stripes match the orientations of the ferroelastic domain walls formed when STO undergoes a cubic to tetragonal phase transition below 105 K [45]. At high densities ($\geq 5 \cdot 10^{14} \text{ cm}^{-2}$) the striped modulations are no longer observed. Interestingly, the threshold carrier density for the disappearance of the stripes coincides with the carrier density resulting in the highest observed mobility. We suggest two possible explanations for the different observations made here with the scanning SQUID:

1. Higher carrier densities should screen potential steps between different structural domains, resulting in small carrier density modulations compared to the total density [44].
2. As the carrier density rises, the degree of bulk conductivity also increases. When the thickness of the conductive layer exceeds the typical thickness of the domains or point defects, additional pathways are formed so the current can bypass the ferroelastic domain walls and thus no modulations in the current densities are observed along the walls.

Overall, the SQUID and transport measurements suggest an increase of the mobility at high carrier density, correlated with screening of scattering sites, up to a point where the bulk conductivity in STO dominates the overall transport.

In the following, we summarize the experimental findings related to the high mobility from this and other studies, and use this as a foundation for the subsequent discussion of the origin. Using pulsed laser deposition, GAO/STO heterostructures with high electron mobility at low temperatures are achieved in a narrow growth window under conditions where both oxygen vacancies and itinerant electrons are located in STO. The Hall mobility was found to be a factor 6 larger than the quantum mobility derived from Shubnikov-de Haas oscillations [3]. Spectroscopic measurements and density functional theory calculations reveal that the breaking of the symmetry at the spinel/perovskite interface creates interface oxygen vacancies with a deeper in-gap state and a lower formation energy compared to oxygen vacancies located deeper in STO [21]. We recently showed that low-temperature annealing (typically $< 100 \text{ }^\circ\text{C}$) can enhance the mobility without altering the carrier density [21]. This, combined with annealing studies of oxygen vacancies in GAO/STO [18], suggests that oxygen vacancies reorder such that the overall scattering decreases. Changing the oxygen vacancy concentration through growth, results in a peak mobility exceeding $100,000 \text{ cm}^2/\text{Vs}$ at a sheet carrier density of $n_s(\mu_{\text{max}}) \sim 4 \cdot 10^{14} \text{ cm}^{-2}$. Above $n_s(\mu_{\text{max}})$, the current flows almost homogeneously in the system and the conductivity gradually increases its three-dimensional character with a concomitant mobility decrease. Below $n_s(\mu_{\text{max}})$, the mobility decreases as $\mu \sim n_s^{1.5}$, and the current flow becomes more inhomogeneous with stripe and point-like modulations, indicative of less electronic screening in the (quasi-) two-dimensionally confined system. GAO also has a smaller lattice mismatch ($\sim 1\%$) with STO than e.g. LAO ($\sim 3\%$), and we note that other high-mobility STO-based heterostructures are also composed of at least one material with a low nominal lattice match, i.e. $\text{La}_{7/8}\text{Sr}_{1/8}\text{MnO}_3$, STO or SrCuO_3 in a-LAO/ $\text{La}_{7/8}\text{Sr}_{1/8}\text{MnO}_3$ /STO [14] with a mobility of $70,000 \text{ cm}^2/\text{Vs}$, STO/ SrCuO_2 /LAO/STO [16] with $50,000$

cm^2/Vs and LAO/STO/STO [15] with $118,000 \text{ cm}^2/\text{Vs}$. At last, one report shows that bands with d_{xz} and d_{yz} symmetry are lower in energy than d_{xy} bands, which is opposite to what is observed for LAO/STO [46]. It remains, however, undemonstrated whether this is the case for high-mobility GAO/STO samples as well.

Whereas a good lattice match with STO might be a prerequisite for obtaining high-mobility STO-based interfaces, we note that obtaining a mobility exceeding that observed in bulk suggests a spatial separation between donors and electrons. Following the spectroscopic and DFT findings in Ref. [21], it seems plausible that oxygen vacancies preferentially accumulate at the spinel/perovskite GAO/STO interface due to the broken symmetry. The electrons distribute deeper into STO owing to the high dielectric constant of STO and the slowly decaying electron distribution in STO [26, 47–49]. If the donor-electron separation is sufficient, the electrons at low concentrations will predominantly be scattered off the unintentional ionized impurities and residual oxygen vacancy donors in STO. In line with the $\mu \sim n_s^{1.5}$ predicted for modulation doping [42, 43], the high electron concentration particularly obtained in GAO/STO could result in a higher mobility by (i) an increase of the Fermi surface with a concomitant small-angle scattering [42] and (ii) a screening of ionized scattering sites and potential variations across domain walls [24]. The momentum relaxation measured via the Hall effect is mostly sensitive to large-angle scattering events, whereas the quantum mobility is sensitive to any scattering event causing phase decoherence. The considerable difference between the Hall and quantum mobility observed at high-mobility GAO/STO is therefore supportive of the preferential small-angle scattering.

At low oxygen growth pressures resulting in $n_s \gg n_s(\mu_{\text{max}})$, oxygen vacancies are present in concentrations exceeding one vacancy pr. STO surface unit cell. At such conditions, the vacancies distribute deep into STO, and the mobility decreases to that observed in bulk conducting STO. The delicate balance between interface and bulk oxygen vacancies naturally leads to a narrow growth window for obtaining high-mobility GAO/STO along with the possibility to alter the mobility by oxygen vacancy redistribution. The maximum mobility obtained when growing half-integer thicknesses of GAO (2.5 unit cells in Ref. [3] and 3.5 unit cells here) appears to originate from the enhanced carrier density at these thicknesses, which, however, remains unaccounted for. Further investigations are also needed to characterize the donor-electron separation suggested by the experimental results here and in Ref. [21]. At present, the oxygen vacancy profile has not yet been investigated directly, whereas studies on the extent of the electron gas suggest that the majority of the electrons are confined within 1.5-7.5 nm from the interface at 10 K [50, 51]. A possible way to investigate the donor-electron separation is to image the depth profile of oxygen vacancies and itinerant electrons using transmission electron microscopy on carefully prepared GAO/STO cross-sections. Density functional theory calculations can also be used to probe whether the TiO_2 layer right at the GAO/STO interface is conducting despite significant distortion from the perovskite/spinel symmetry breaking, large amounts of oxygen vacancies and significant interdiffusion of Al into the first 1-2 unit cells of STO [3]. Lastly, a systematic study of how the ratio between quantum and Hall mobility depends on the carrier density would be interesting to check the hypothesis on decreasing the scattering angle when the carrier density increases. Such a study may, however, be challenging as the Shubnikov-de Haas oscillations resides on a large magnetoresistive background [3].

Conclusion:

In conclusion, we have investigated the mobility in GAO/STO by varying the carrier density via control of the growth parameters and post-deposition annealing. We find that for all investigated carrier densities, the mobility at $T > 150$ K is dominated by optical phonon scattering. High mobility (~ 12 cm²/Vs) is found for high carrier densities where the electron-phonon coupling is weak and the effective polaron mass is small. At intermediate temperatures, the experimental findings are consistent with electron-electron scattering. At low temperatures, the mobility exceeds 100.000 cm²/Vs at a sheet carrier density of around $4 \cdot 10^{14}$ cm⁻². The optimum appears to be a delicate balance between, on one hand, the enhanced screening and small-angle scattering occurring at high carrier densities and, on the other hand, the bulk conductivity arising when oxygen vacancies are formed deep into STO. Indeed, we find that $\mu \sim n_s^{1.5}$ at lower carrier densities whereas at high densities the mobility is reduced to that of bulk conducting STO. The study paves the way for designing and reproducing all-oxide material platforms with high electron mobility. There are several interesting perspectives of the present study on achieving high mobility in GAO/STO:

1. One of the aspects of STO-based heterostructures that has attracted much attention is that the carrier density is several orders of magnitude higher than for typical high-mobility two-dimensional electron gases in conventional semiconductors. In the case of GAO/STO, we observe high mobility at carrier densities one order of magnitude higher than typical LAO/STO heterostructures, which leads to sheet resistances less than 0.1 Ω at 2 K and very low Joule losses.
2. A high quantum mobility opens up for the possibility to study quantum coherence in nanoscale devices such as the Aharonov-Bohm interferometer.
3. The electronic properties are found to be highly influenced by the domain walls of ferroelastic STO, which can be controlled using electric fields and strain [44, 45]. The domain walls may therefore be used to design nanoelectronics with writable, erasable and movable properties.
4. The high mobility in GAO/STO offers the possibility of realizing so-called extraordinary magnetoresistance in oxide/metal hybrid devices [52]. In the absence of a magnetic field, the current in such extraordinary magnetoresistive devices primarily flows in the metallic regions, which leads to a low resistance. However, when a magnetic field is applied to a device with high carrier mobility, the Lorentz force deflects the current away from the metallic regions, resulting in a large positive magnetoresistance. GAO/STO may be particularly promising for designing such extraordinary magnetoresistive devices at low temperatures as it combines two important properties: First, GAO/STO has a high mobility, giving a low resistance in the absence of a magnetic field and an efficient Lorentz deflection in the presence of a magnetic field [53, 54]. Second, even in the absence of metal inclusions, the GAO/STO heterostructure already shows a very high positive magnetoresistance. Adding geometrically optimized metal inclusions to GAO/STO may lead to an exceptionally high magnetoresistance by combining the intrinsic high magnetoresistance of GAO/STO with the extraordinary magnetoresistance stemming from the geometrical enhancement.

Acknowledgement:

PS and RC gratefully acknowledge support by the Deutsche Forschungsgemeinschaft through SFB 1170 *ToCoTronics*.

Additional Information:

Competing financial interests: The authors declare no competing financial interests.

1. V. Umansky, M. Heiblum, Y. Levinson, J. Smet, J. Nübler, and M. Dolev, MBE growth of ultra-low disorder 2DEG with mobility exceeding $35 \times 10^6 \text{ cm}^2/\text{Vs}$, *J. Cryst. Growth* 311, 1658 (2009).
2. J. Falson, Y. Kozuka, M. Uchida, J. H. Smet, T. Arima, A. Tsukazaki, and M. Kawasaki, MgZnO/ZnO heterostructures with electron mobility exceeding $1 \times 10^6 \text{ cm}^2/\text{Vs}$, *Sci. Rep.* 6, 26598 (2016).
3. Y. Z. Chen, N. Bovet, F. Trier, D. V. Christensen, F. M. Qu, N. H. Andersen, T. Kasama, W. Zhang, R. Giraud, J. Dufouleur, T. S. Jespersen, J. R. Sun, A. Smith, J. Nygård, L. Lu, B. Büchner, B. G. Shen, S. Linderoth, and N. Pryds, A high-mobility two-dimensional electron gas at the spinel/perovskite interface of $\gamma\text{-Al}_2\text{O}_3/\text{SrTiO}_3$, *Nat. Commun.* 4, 1371 (2013).
4. W. D. Rice, P. Ambwani, M. Bombeck, J. D. Thompson, G. Haugstad, C. Leighton, and S. A. Crooker, Persistent optically induced magnetism in oxygen-deficient strontium titanate, *Nat. Mater.* 13, 481 (2014).
5. H.-M. Christen, J. Mannhart, E. J. Williams, and C. Gerber, Dielectric properties of sputtered SrTiO_3 films, *Phys. Rev. B* 49, 12095 (1994).
6. E. Sawaguchi, A. Kikuchi, and Y. Kodera, Dielectric Constant of Strontium Titanate at Low Temperatures, *J. Phys. Soc. Jpn.* 17, 1666 (1962).
7. E. Mikheev, B. Himmetoglu, A. P. Kajdos, P. Moetakef, T. A. Cain, C. G. Van de Walle, and S. Stemmer, Limitations to the room temperature mobility of two- and three-dimensional electron liquids in SrTiO_3 , *Appl. Phys. Lett.* 106, 062102 (2015).
8. H. P. R. Frederikse and W. R. Hosler, Hall Mobility in SrTiO_3 , *Phys. Rev.* 161, 822 (1967).
9. O. N. Tuftte and P. W. Chapman, Electron mobility in semiconducting strontium titanate, *Phys. Rev.* 155, 796 (1967).
10. J. Son, P. Moetakef, B. Jalan, O. Bierwagen, N. J. Wright, R. Engel-Herbert, and S. Stemmer, Epitaxial SrTiO_3 films with electron mobilities exceeding $30,000 \text{ cm}^2\text{V}^{-1}\text{s}^{-1}$, *Nat. Mater.* 9, 482 (2010).
11. B. Jalan, S. J. Allen, G. E. Beltz, P. Moetakef, and S. Stemmer, Enhancing the electron mobility of SrTiO_3 with strain, *Appl. Phys. Lett.* 98, 132102 (2011).
12. Y. Matsubara, K. S. Takahashi, M. S. Bahramy, Y. Kozuka, D. Maryenko, J. Falson, A. Tsukazaki, Y. Tokura, and M. Kawasaki, Observation of the quantum Hall effect in δ -doped SrTiO_3 , *Nat. Commun.* 7, 11631 (2016).
13. B. Jalan, S. Stemmer, S. Mack, and S. J. Allen, Two-dimensional electron gas in δ -doped SrTiO_3 , *Phys. Rev. B* 82, 081103 (2010).
14. Y. Z. Chen, F. Trier, T. Wijnands, R. J. Green, N. Gauquelin, R. Egoavil, D. V. Christensen, G. Koster, M. Huijben, N. Bovet, S. Macke, F. He, R. Sutarto, N. H. Andersen, J. A. Sulpizio, M. Honig, G. E. D. K. Prawiroatmodjo, T. S. Jespersen, S. Linderoth, S. Ilani, J. Verbeeck, G. Van Tendeloo, G. Rijnders, G. A. Sawatzky, and N. Pryds, Extreme mobility enhancement of two-dimensional electron gases at oxide interfaces by charge-transfer-induced modulation doping, *Nat. Mater.* 14, 801 (2015).
15. A. David, Y. Tian, P. Yang, X. Gao, W. Lin, A. B. Shah, J.-M. Zuo, W. Prellier, and T. Wu, Colossal positive magnetoresistance in surface-passivated oxygen-deficient strontium titanate, *Sci. Rep.* 5, 10255 (2015).
16. M. Huijben, G. Koster, M. K. Kruize, S. Wenderich, J. Verbeeck, S. Bals, E. Slooten, B. Shi, H. J. A. Molegraaf, J. E. Kleibeuker, S. van Aert, J. B. Goedkoop, A. Brinkman, D. H. A. Blank, M. S. Golden, G. van Tendeloo, H. Hilgenkamp, and G. Rijnders, Defect Engineering in Oxide Heterostructures by Enhanced Oxygen Surface Exchange, *Adv. Funct. Mater.* 23, 5240 (2013).
17. F. Gunkel, S. Hoffmann-Eifert, R. Dittmann, S. B. Mi, C. L. Jia, P. Meuffels, and R. Waser, High temperature conductance characteristics of $\text{LaAlO}_3/\text{SrTiO}_3$ -heterostructures under equilibrium oxygen atmospheres, *Appl. Phys. Lett.* 97, 012103 (2010).
18. D. V. Christensen, M. von Soosten, F. Trier, T. S. Jespersen, A. Smith, Y. Chen, and N. Pryds, Controlling the carrier density of SrTiO_3 -based heterostructures with annealing, *Adv. Electron. Mater.* 1700026 (2017).

19. F. Trier, K. V. Reich, D. V. Christensen, Y. Zhang, H. L. Tuller, Y. Chen, B. I. Shklovskii, and N. Pryds, Universality of electron mobility in $\text{LaAlO}_3/\text{SrTiO}_3$ and bulk SrTiO_3 , *Appl. Phys. Lett.* **111**, 092106 (2017).
20. T. D. Sanders, M. T. Gray, F. J. Wong, and Y. Suzuki, $\text{LaAlO}_3/\text{SrTiO}_3$ interfaces doped with rare-earth ions, *Phys. Rev. B* **91**, 205112 (2015).
21. P. Schütz, D. V. Christensen, V. Borisov, F. Pfaff, P. Scheiderer, L. Dudy, M. Zapf, J. Gabel, Y. Z. Chen, N. Pryds, V. A. Rogalev, V. N. Strocov, T.-L. Lee, H. O. Jeschke, R. Valentí, M. Sing, and R. Claessen, Microscopic origin of the mobility enhancement at a spinel/perovskite oxide heterointerface revealed by photoemission spectroscopy, *Phys. Rev. B* **96**, 161409 (2017).
22. D. V. Christensen, F. Trier, M. von Soosten, G. E. D. K. Prawiroatmodjo, T. S. Jespersen, Y. Z. Chen, and N. Pryds, Electric field control of the $\gamma\text{-Al}_2\text{O}_3/\text{SrTiO}_3$ interface conductivity at room temperature, *Appl. Phys. Lett.* **109**, 021602 (2016).
23. A. Joshua, S. Pecker, J. Ruhman, E. Altman, and S. Ilani, A universal critical density underlying the physics of electrons at the $\text{LaAlO}_3/\text{SrTiO}_3$ interface, *Nat. Commun.* **3**, 1129 (2012).
24. C. Hamaguchi, *Basic semiconductor physics*, Berlin, Heidelberg, Springer Berlin Heidelberg (2010).at <<http://link.springer.com/10.1007/978-3-642-03303-2>>
25. A. Verma, A. P. Kajdos, T. A. Cain, S. Stemmer, and D. Jena, Intrinsic Mobility Limiting Mechanisms in Lanthanum-Doped Strontium Titanate, *Phys. Rev. Lett.* **112**, 216601 (2014).
26. S. Su, J. Ho You, and C. Lee, Electron transport at interface of LaAlO_3 and SrTiO_3 band insulators, *J. Appl. Phys.* **113**, 093709 (2013).
27. C. Cancellieri, A. S. Mishchenko, U. Aschauer, A. Filippetti, C. Faber, O. S. Barišić, V. A. Rogalev, T. Schmitt, N. Nagaosa, and V. N. Strocov, Polaronic metal state at the $\text{LaAlO}_3/\text{SrTiO}_3$ interface, *Nat. Commun.* **7**, 10386 (2016).
28. X. Lin, C. W. Rischau, L. Buchauer, A. Jaoui, B. Fauque, and K. Behnia, Metallicity without quasi-particles in room-temperature strontium titanate, *ArXiv Prepr. ArXiv170207144* (2017).at <<https://arxiv.org/abs/1702.07144>>
29. F. E. Low and D. Pines, Mobility of slow electrons in polar crystals, *Phys. Rev.* **98**, 414 (1955).
30. Z. Wang, S. McKeown Walker, A. Tamai, Y. Wang, Z. Ristic, F. Y. Bruno, A. de la Torre, S. Riccò, N. C. Plumb, M. Shi, P. Hlawenka, J. Sánchez-Barriga, A. Varykhalov, T. K. Kim, M. Hoesch, P. D. C. King, W. Meevasana, U. Diebold, J. Mesot, B. Moritz, T. P. Devereaux, M. Radovic, and F. Baumberger, Tailoring the nature and strength of electron–phonon interactions in the $\text{SrTiO}_3(001)$ 2D electron liquid, *Nat. Mater.* **15**, 835 (2016).
31. F. M. Peeters, X. Wu, and J. T. Devreese, Exact and approximate results for the mass of a two-dimensional polaron, *Phys. Rev. B* **37**, 933 (1988).
32. G. Herranz, M. Basletić, M. Bibes, C. Carrétéro, E. Tafra, E. Jacquet, K. Bouzehouane, C. Deranlot, A. Hamzić, J.-M. Broto, A. Barthélémy, and A. Fert, High Mobility in $\text{LaAlO}_3/\text{SrTiO}_3$ Heterostructures: Origin, Dimensionality, and Perspectives, *Phys. Rev. Lett.* **98**, 216803 (2007).
33. F. E. Low and D. Pines, The Mobility of Slow Electrons in Polar Crystals, *Phys. Rev.* **91**, 193 (1953).
34. A. S. Barker Jr, Temperature Dependence of the Transverse and Longitudinal Optic Mode Frequencies and Charges in SrTiO_3 and BaTiO_3 , *Phys. Rev.* **145**, 391 (1966).
35. C. Lee, J. Yahia, and J. L. Brebner, Electronic conduction in slightly reduced strontium titanate at low temperatures, *Phys. Rev. B* **3**, 2525 (1971).
36. T. Okuda, K. Nakanishi, S. Miyasaka, and Y. Tokura, Large thermoelectric response of metallic perovskites: $\text{Sr}_{1-x}\text{La}_x\text{TiO}_3$ ($0 \leq x \leq 0.1$), *Phys. Rev. B* **63**, 113104 (2001).
37. D. van der Marel, J. L. M. van Mechelen, and I. I. Mazin, Common Fermi-liquid origin of T^2 resistivity and superconductivity in n-type SrTiO_3 , *Phys. Rev. B* **84**, 205111 (2011).
38. E. Mikheev, S. Raghavan, J. Y. Zhang, P. B. Marshall, A. P. Kajdos, L. Balents, and S. Stemmer, Carrier density independent scattering rate in SrTiO_3 -based electron liquids, *Sci. Rep.* **6**, 20865 (2016).

39. S. N. Klimin, J. Tempere, D. van der Marel, and J. T. Devreese, Microscopic mechanisms for the Fermi-liquid behavior of Nb-doped strontium titanate, *Phys. Rev. B* 86, 045113 (2012).
40. X. Lin, B. Fauqué, and K. Behnia, Scalable T^2 resistivity in a small single-component Fermi surface, *Science* 349, 945 (2015).
41. M. Swift and C. G. Van de Walle, Conditions for T^2 resistivity from electron-electron scattering, *ArXiv Prepr. ArXiv170104744* (2017).at <<https://arxiv.org/abs/1701.04744>>
42. D. Monroe, Comparison of mobility-limiting mechanisms in high-mobility $\text{Si}_{1-x}\text{Ge}_x$ heterostructures, *J. Vac. Sci. Technol. B Microelectron. Nanometer Struct.* 11, 1731 (1993).
43. X. Mi, T. M. Hazard, C. Payette, K. Wang, D. M. Zajac, J. V. Cady, and J. R. Petta, Magnetotransport studies of mobility limiting mechanisms in undoped Si/SiGe heterostructures, *Phys. Rev. B* 92, 035304 (2015).
44. M. Honig, J. A. Sulpizio, J. Drori, A. Joshua, E. Zeldov, and S. Ilani, Local electrostatic imaging of striped domain order in $\text{LaAlO}_3/\text{SrTiO}_3$, *Nat. Mater.* 12, 1112 (2013).
45. B. Kalisky, E. M. Spanton, H. Noad, J. R. Kirtley, K. C. Nowack, C. Bell, H. K. Sato, M. Hosoda, Y. Xie, Y. Hikita, C. Woltmann, G. Pfanzelt, R. Jany, C. Richter, H. Y. Hwang, J. Mannhart, and K. A. Moler, Locally enhanced conductivity due to the tetragonal domain structure in $\text{LaAlO}_3/\text{SrTiO}_3$ heterointerfaces, *Nat. Mater.* 1 (2013).doi:10.1038/nmat3753
46. Y. Cao, X. Liu, P. Shafer, S. Middey, D. Meyers, M. Kareev, Z. Zhong, J.-W. Kim, P. J. Ryan, E. Arenholz, and others, Anomalous orbital structure in a spinel-perovskite interface, *Npj Quantum Mater.* 1, 16009 (2016).
47. W. Son, E. Cho, B. Lee, J. Lee, and S. Han, Density and spatial distribution of charge carriers in the intrinsic n-type $\text{LaAlO}_3\text{-SrTiO}_3$ interface, *Phys. Rev. B* 79, 245411 (2009).
48. Y. Yamada, H. K. Sato, Y. Hikita, H. Y. Hwang, and Y. Kanemitsu, Spatial density profile of electrons near the $\text{LaAlO}_3/\text{SrTiO}_3$ heterointerface revealed by time-resolved photoluminescence spectroscopy, *Appl. Phys. Lett.* 104, 151907 (2014).
49. K. V. Reich, M. Schechter, and B. I. Shklovskii, Accumulation, inversion, and depletion layers in SrTiO_3 , *Phys. Rev. B* 91, 115303 (2015).
50. P. Schütz, F. Pfaff, P. Scheiderer, Y. Z. Chen, N. Pryds, M. Gorgoi, M. Sing, and R. Claessen, Band bending and alignment at the spinel/perovskite $\gamma\text{-Al}_2\text{O}_3/\text{SrTiO}_3$ heterointerface, *Phys. Rev. B* 91, 165118 (2015).
51. M. Yazdi-Rizi, P. Marsik, B. P. P. Mallett, A. Dubroka, D. V. Christensen, Y. Z. Chen, N. Pryds, and C. Bernhard, Infrared ellipsometry study of the confined electrons in a high-mobility $\gamma\text{-Al}_2\text{O}_3/\text{SrTiO}_3$ heterostructure, *EPL Europhys. Lett.* 113, 47005 (2016).
52. S. A. Solin, T. Thio, D. R. Hines, and J. J. Heremans, Enhanced room-temperature geometric magnetoresistance in inhomogeneous narrow-gap semiconductors, *Science* 289, 1530 (2000).
53. M. Holz, O. Kronenwerth, and D. Grundler, Magnetoresistance of semiconductor-metal hybrid structures: The effects of material parameters and contact resistance, *Phys. Rev. B* 67 (2003).
54. J. Sun and J. Kosel, Extraordinary Magnetoresistance in Semiconductor/Metal Hybrids: A Review, *Materials* 6, 500 (2013).

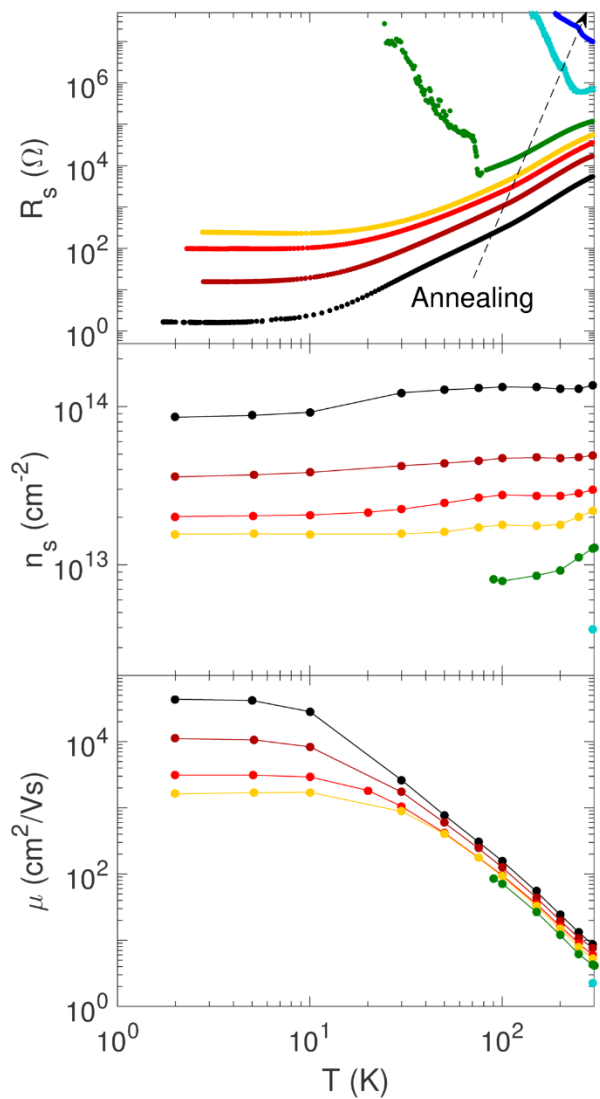


Figure 1: Sheet resistance (R_s), Hall sheet carrier density (n_s) and Hall electron mobility (μ) as a function of temperature for a single γ - $\text{Al}_2\text{O}_3/\text{SrTiO}_3$ heterostructure at various annealing steps. The heterostructure is annealed in 1 bar pure oxygen at ~ 200 °C for 2-8 hours between each Hall measurement, which causes a monotonous decrease in the carrier density from $1 \cdot 10^{14} \text{ cm}^{-2}$ (black) to $3 \cdot 10^{12} \text{ cm}^{-2}$ (cyan). All lines are guide to the eye.

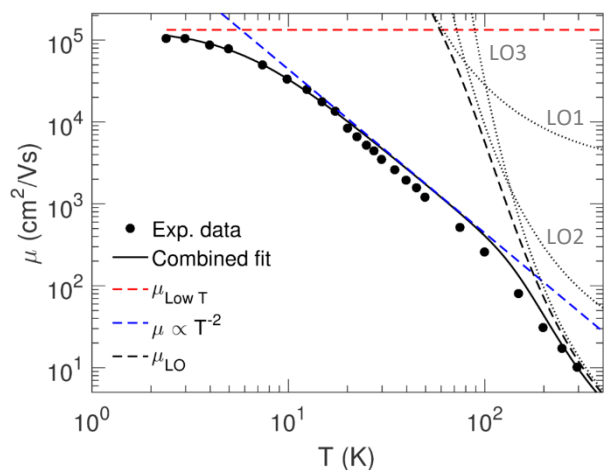


Figure 2: Electron mobility as a function of temperature where two fitting parameters are used describe the three contributions to the mobility according to Eq. (3). LO1-3 describes the three longitudinal optical phonon modes. Note that the data originate from a sample that was not post-deposition annealed.

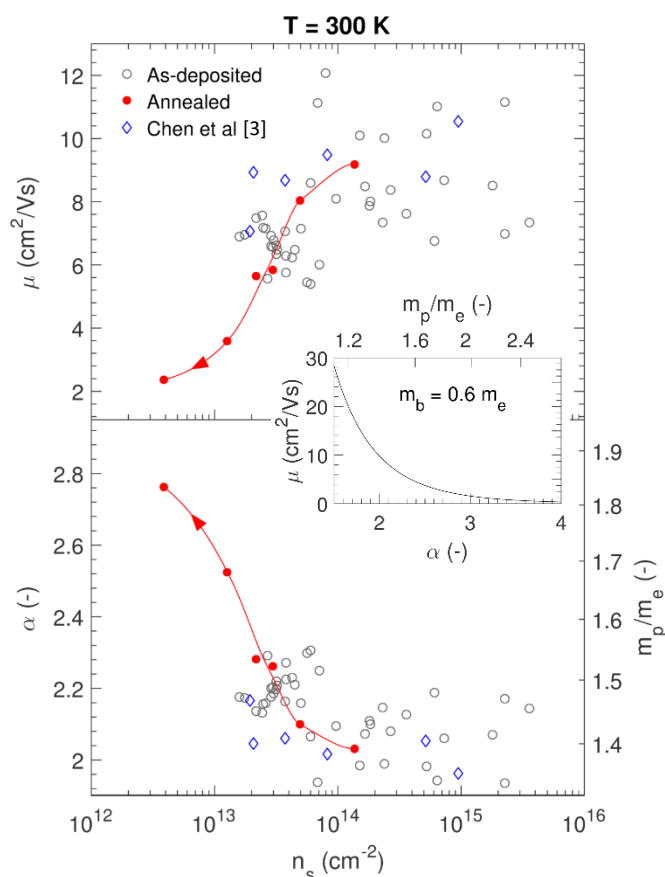


Figure 3: Top: Room temperature electron mobility (μ) as a function of carrier density (n_s) for as-deposited and post-annealed GAO/STO. Note that data for as-deposited GAO/STO by Chen et al [3] is also included. Bottom: Electron-phonon coupling (α) and polaron effective mass (m_p) as a function of the carrier density. Inset: The mobility as a function of the electron-phonon coupling as calculated from Eq. (4) assuming a band effective mass of $m_b=0.6m_e$ and two-dimensional polarons. The red lines are guides to the eye.

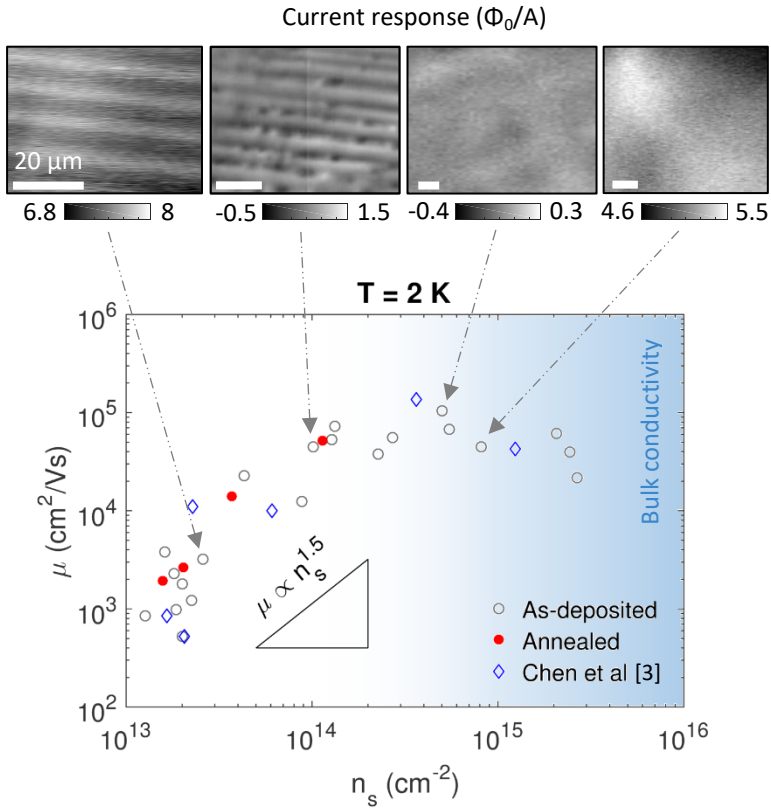


Figure 4: Electron mobility (μ) as a function of the sheet carrier density (n_s) at 2 K for as-deposited GAO/STO, post-deposition annealed GAO/STO and as-deposited GAO/STO from Chen et al [3]. For four samples with varying carrier density, the scanning SQUID images show the magnetic flux created by the current flow in the samples. Occasionally, the current flow in low-density GAO/STO samples show areas with scattered points of local (resolution limited) reduction in the current density, probably related to point defects or defect clusters. Such an area is presented in the second scanning SQUID image, but similar areas are found in the sample with the low carrier density. Note that the absolute value of the magnetic flux measured on different samples cannot be directly compared as it depends on the position on the sample. The scale bars are 20 μm in all the images.